Nuclear Materials and Energy 34 (2023) 101319

Contents lists available at ScienceDirect

Nuclear Materials and Energy

journal homepage: www.elsevier.com/locate/nme

Energy load on first wall components in high density, small ELM regimes in ASDEX Upgrade

A. Redl [a,*], T. Eich [b], N. Vianello [c,d], P. David [b], the ASDEX Upgrade Team [1], the EUROfusion MST1 Team [2]

[a] Department of Economics, Engineering, Society and Business Organization (DEIM), University of Tuscia, Largo dell'Universit'a snc, 01100 Viterbo, Italy
[b] Max–Planck-Institute for Plasma Physics, Boltzmannstr.2, 85748 Garching, Germany
[c] Consorzio RFX (CNR, ENEA, INFN, Universitá di Padova, Acciaierie Venete SpA), Corso Stati Uniti 4, 35127 Padova, Italy
[d] Istituto per la Scienza e la Tecnologia dei Plasmi, CNR, Corso Stati Uniti 4, 35127 Padova, Italy

ARTICLE INFO

Keywords:
ASDEX Upgrade
Calorimetric measurements
QCE regime
Power Exhaust

ABSTRACT

A set of dedicated shots with constant heating power combining NBI (Neutral Beam Injection) and ECRH (Electron Cyclotron Resonance Heating) have been executed at the ASDEX Upgrade (AUG) tokamak using a highly shaped small ELM magnetic geometry in order to investigate the differences on heat loads at the first wall of AUG by means of the revised cooling water calorimetry. The flattop fuelling has been varied on a shot-to-shot basis while keeping constant all the other parameters, exploring a large range of the density operational space of AUG. Reducing the fuelling rate allows a gradual transition from small ELM regime at high density into a Type-I ELMy H-mode. Additionally, the safety factor q has been increased/decreased by changing B_{tor}, which leads also to variations in the heating scheme. With the lowest flattop fuelling, reaching a Type-I ELMy H-mode, a fraction of $\sim$ 6% of calorimetrically captured energy loads at the first wall normalized against the entire calorimetrically captured energy has been recorded, whereas in the highest fuelling case, being in a small ELM scenario, the first wall heat loads are increased up to 16%. Considering all cases reveals an almost linear trend between the fraction of energy deposited at the first wall and the turbulence control parameter α_t. This observation is consistent with an enhancement of the filamentary activity at higher α_t, when the plasma turbulence is dominated by resistive interchange modes at the separatrix.

1. Introduction

The proper handling of the power exhaust reaching the plasma-facing components (PFCs), in particular of the divertor region, represents one of the major difficulties in view of the commercial exploitation of a possible fusion reactor. The standard parameter used to determine the steady state heat loads on the divertor tiles is the exponential decay length λ_q [1], which is obtained by infrared (IR) thermography measurements at the outer target. This parameter describes the width of the power-carrying layer outside the separatrix. An empirical ITPA multi-machine scaling obtained in attached conditions [2] predict an inter-ELM value of λ_q for ITER of $\sim$ 1 mm leading to new challenges for PFC materials. Furthermore, the transient heat loads on the first wall caused by Type-I ELMs [3] will reduce the lifetime of first wall PFCs and has to be controlled by mitigation or suppression in ITER [4–6] and avoided in any future fusion reactors [7].

Several scenarios which attempt to handle the power exhaust challenge by exploiting different approaches are under investigations. One of those candidates is the so-called 'Quasi-Continuous-Exhaust' (QCE) regime [8]. This scenario combines high plasma core density (close to 1.0 n_{GW} [9]) and high separatrix density (up to 0.6 n_{GW} with gas fuelling only) at high triangularity, close to double-null shaping. Beside the relevance of high $n_{e,sep}$ in order to achieve high radiative losses and divertor detachment which is needed to reduce peak heat fluxes and surface erosion on PCFs [10], it plays a key role to reach plasma boundaries in which Type-I ELMs are replaced by smaller ELMs. Due to the presence of an enhanced filamentary transport, a broadening of the λ_q is observed with an increased energy deposition outside the divertor [8,11,12]. A previous study has indicated that an increased heat load deposition at the upper divertor is observed with IR measurements [8]. Heat load measurements on further non-divertor components are still pending.

* Corresponding author.
E-mail address: Andreas.Redl@unitus.it (A. Redl).
[1] See author list of Stroth et al. 2022 Nucl. Fusion **62** 042006.
[2] See author list of Labit et al. 2019 Nuclear Fusion **59** 086020.

https://doi.org/10.1016/j.nme.2022.101319
Received 29 June 2022; Received in revised form 21 November 2022; Accepted 28 November 2022
Available online 9 December 2022

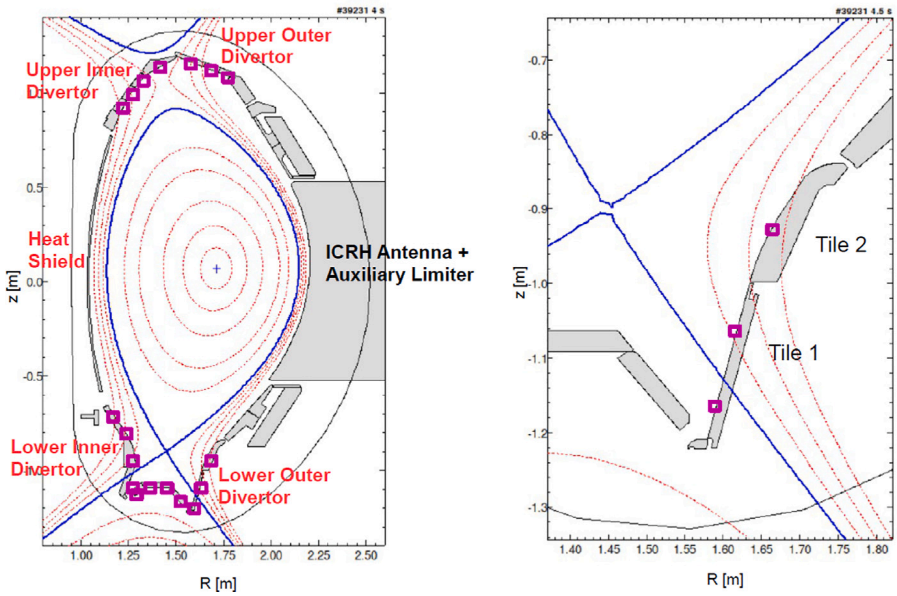

Fig. 1. Left: Poloidal cross section of the ASDEX Upgrade tokamak indicating the coverage of the cooling units (indicated as red/black labels) available through the revised cooling water calorimetry and the thermocouples. The calorimetry provides an almost perfect toroidal and poloidal coverage of the AUG in-vessel components. Each purple marker indicates one thermocouple providing a poloidal coverage of the lower/upper divertor in single segments of AUG. The small ELM equilibrium shown in the left plot is used for the entire database presented in this study. Right: Close-up of the outer divertor with the reference equilibrium. The positions of the thermocouples available at the lower target are indicated. The main outer target is labelled as 'Tile 1' and the additional row of tiles in the lower outer divertor is labelled as 'Tile 2'. (For interpretation of the references to colour in this figure legend, the reader is referred to the web version of this article.)

This scenario combines features that could be of interest for ITER or future fusion reactors. However, to date, the extent of first-wall heat loads due to the enhanced filamentary transport is not known yet, which may lead to new challenges for the PFC material of non-divertor components in the worst-case scenario. It is known from previous works in L-modes at AUG [13] that filamentary transport may carry a significant amount of energy, leading to increased energy deposition on non-divertor components. Until now, reliable calorimetric measurements of the first wall, or to be more general, of all in-vessel components have been missing. The IR thermography, which is typically used to measure heat fluxes at outer targets, has limited applicability at the first wall. A first attempt with IR-measurements was made in AUG with carbon walls in 2004 to estimate heat loads on non-divertor components [14]. In a low-density ELMy H-mode, it was estimated that about 5% of the heat loads were found at the first wall of AUG.

In order to measure these heat loads at non-divertor components, two outdated calorimetric diagnostics available at AUG have been completely revised and recommissioned [15,16]. The cooling water calorimetry (KWK) provides measurements on almost all AUG in-vessel components. In addition, the lower and upper divertor tiles are equipped with thermocouples, which covers poloidally the entire upper/lower divertor in individual segments and provides tile-resolved heat distributions. The aim of this work is to measure the first wall heat load of discharges with dedicated boundaries and to report on the dependence of the first wall heat loads on separatrix conditions.

The paper is structured as follow: in Section 2, the two main calorimetric diagnostics and the experimental setup of the executed shots are briefly introduced. In Section 3, the calorimetric results of the dedicated database is shown and results on scaling the the first wall heat loads in AUG are presented. Section 4 contains the summary and the next steps.

2. Experimental setup for scaling the first wall heat loads

2.1. Latest calorimetric diagnostics available at AUG

For the determination of the heat loads on any PCFs, the revised cooling water calorimetry of AUG has been used. The calorimetry is based on the extensive AUG cooling system covering the entire machine and provides an almost perfect toroidal and poloidal coverage of all in-vessel components in AUG. In this system certain areas are cumulated into so-called "cooling units" and are the smallest spatial units to resolve heat loads. It can resolve the heat shield, upper inner/outer divertor and the lower inner/outer divertor in all 16 toroidal segments. These cooling units are indicated as red labels in Fig. 1 (left) and in sum 80 cooling units are available. The ICRH (Ion Cyclotron Resonance Heating) antennas and auxiliary limiters adjacent to the NBI ducts are also connected to the cooling systems, and each component provides individual heat load measurements. These cooling units in the limiter are indicated as black labels in Fig. 1 (left) and are in sum 8 cooling units. In sum, 88 cooling units are available through the AUG cooling water calorimetry. In order to determine the acquired heat loads per cooling unit Q, one has to solve the formula as given in Ref. [17]:

$$Q = m \int_{t_1}^{t_2} \Delta T c_p dt, \quad (1)$$

where m denotes the flow rate of a cooling unit, ΔT the relative rise obtained from the difference of the inlet and outlet cooling water temperature, c_p is the heat capacity of the cooling water and the time interval $[t_1, t_2]$ covers the full excursion of the relative temperature profile ΔT. The discharge duration of an AUG experiment has a maximum of 10 s, which is much smaller than the heat conduction time for the in-vessel components, which only allows to measure the temperature signals during the cooling-down phase. Due to this and according to Eq. (1) Q is time-integrated and no real-time data is available.

As an additional calorimetric diagnostic, the extensive wall thermometry of AUG [17] is used in order to increase the spatial resolution for calorimetric measurements. It consists of 94 thermocouples covering poloidally important areas of in-vessel components, mainly the lower (segments 4, 8, 10 and 13) and upper divertor (segments 4 and 13). In the AUG tokamak, one tile is equipped with one thermocouple, except for the full tungsten tiles in the lower outer divertor. In this case, two thermocouples are installed in one tile. For the calorimetric evaluation, the mean value of these two profiles is used, like it is done in Ref. [18]. The calorimetric evaluation of the AUG thermocouples

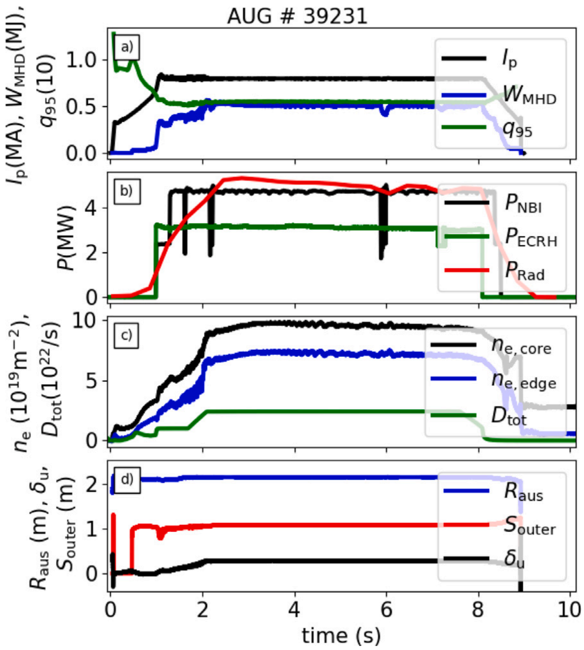

Fig. 2. Experimental time traces of relevant plasma parameters of AUG discharge #39231. Panel (a) presents the plasma current I_p(black), W_{MHD}(blue) and q_{95}(green). Panel (b) presents the heating scheme combining NBI(black) and ECRH(green) in X2-mode at B_{tor}=−2.45T. For B_{tor}=−1.8T, the ECRH contribution is switched to X3-mode, whereas for B_{tor}=−2.8T the ECRH contribution is replaced by one additional NBI source. Radiation losses P_{rad}(red) are calculated by BPT [21]. In panel (c), the line-integrated density of core(black) and edge(blue) is shown. The total fuelling rate D_{tot} is also added. Panel (d) presents the traces of R_{aus}, the strikeline position at the outer target S_{outer} and the upper triangularity δ_u. (For interpretation of the references to colour in this figure legend, the reader is referred to the web version of this article.)

is based on the approach described in Ref. [18], but adjusted for the boundaries given in the AUG tokamak and allows to calculate the thermal energy stored in the tile according to formula

$$Q = m_{tile} \int c_p(T) dT, \quad (2)$$

where m_{tile} is the mass of the tile, c_p(T) is the temperature-dependent heat capacity and the boundaries of the integral define the temperature rise. Fit formulae for the temperature-dependent heat capacities are taken from results in Refs. [19,20]. As the so-called 'tile calorimetry' approach requires thermal equilibrium, and according to Eq. (2) Q is time-integrated, no real-time data is available.

2.2. Experimental setup of the small-ELM database

Two calorimetric diagnostics, which are able to measure heat loads on any PFCs of AUG, have been briefly introduced. The boundaries caused by the calorimetric diagnostics lead to a specific discharge configuration and database. In order to be able to align the measured heat loads to dedicated plasma parameters, each discharge is kept as constant as possible during its execution. All shots, which have been executed for this study, have the same magnetic equilibrium with high upper triangularity δ_u (close to double-null). The shape can be seen in Fig. 1 (left). From Fig. 2 panel (d), one can see the traces of R_{aus} (R-coordinate of outer separatrix at the midplane level), δ_u and the strikeline position on the outer target S_{outer}. In order to provide a robust scaling parameter, the safety factor q has been varied by changing B_{tor}. For the database, shots have been executed at three different B_{tor}-values: −2.45T, −1.8T and −2.8T. Due to different q-values, different heating schemes have to be used. Panel (b) of Fig. 2 shows the heating scheme for B_{tor}=−2.45T. In case of B_{tor}=−1.8T, the ECRH is used in X3-mode (and just with 3 gyrotrons). For the highest B_{tor}-value, the ECRH contribution is replaced by an additional NBI source. The ECRH contribution is directed as 'central heating'. Using different heating schemes allows to prove that the scaling of heat loads does not depend directly on the heating scheme, but rather on plasma parameters like the electron temperature T_e in the core or the separatrix. To cover a large area of the operational space, the fuelling level in the flattop phase has been varied in each shot. Panel (c) shows the fuelling level in the flattop phase for reference shot #39231 at 2.5e22/s. In case of B_{tor}=−2.45T, the flattop fuelling covers a range between 0.1e22/s and 2.85e22/s in several shots. The upper fuelling value was limited by the ECRH cut-off density. At lower fuelling levels (≤ 0.6e22/s) a transition from the small ELM regime to a Type-I ELMy H-mode [22] has been observed. At B_{tor}=−2.8T a range between 1.75e22/s and 3.2e22/s is covered in several shots and at B_{tor}=−1.8T a range between 1.0e22/s and 3.2e22/s is covered in several shots. Where the range of different B_{tor}-values covers each other, the same flattop fuelling levels have been used.

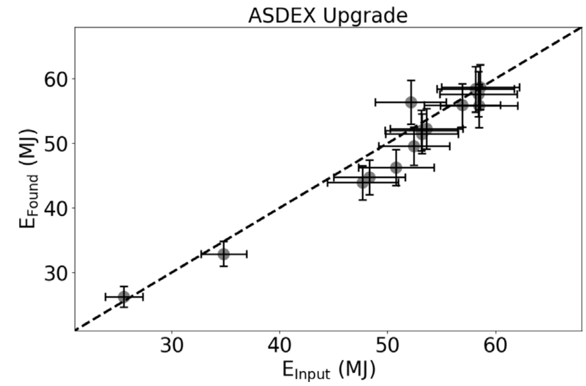

Fig. 3. The plot presents the global energy balance obtained with the AUG cooling water calorimetry for the presented database. The injected and found energy matches over the entire range almost perfectly. The approach presented here is extensively desribed in Ref. [16].

3. Empirical scaling of the first wall heat loads in AUG

Before we can try to scale the heat loads on any PFCs in AUG, we have to prove that the calorimetry provides reasonable values regarding the global energy balance. Having a reasonable global energy balance ensures that (almost) all heat loads are properly captured and one can trust the distributions obtained with the KWK. In Fig. 3, the global energy balance of the small ELM database is presented. Over the entire range, the injected and measured energy matches almost perfectly. Applying a linear regression on that database, reveals that 97.5% is found on average. The two outliers at ∼ 28MJ and ∼ 36MJ are shots which were prematurely terminated without the use of killergas. The use of killergas would falsify the energy distribution on any PFCs, which has to be avoided for this study. For further information on setting up the global energy balance or the revised cooling water calorimetry in AUG, we refer to Refs. [15,16].

Having such a promising balance provides a reliable scaling on any PCFs of AUG. We will concentrate on the first wall trying to infer the differences in first wall heat load moving from Type-I ELMy regimes to high density small ELM regimes.

For the scaling of the heat loads of the first wall, dedicated cooling units are foreseen. According to the results in Ref. [14], the first wall is represented by the four ICRH antennas and the four auxiliary limiters, which are installed on the left and right side of both NBI ducts. According to the observations in Ref. [14], Type-I ELMs reach the auxiliary limiters, therefore this areas has to be taken into account. In sum, 8 cooling units define the first wall. The sum of these heat loads are normalized against the sum of all 88 cooling units provided

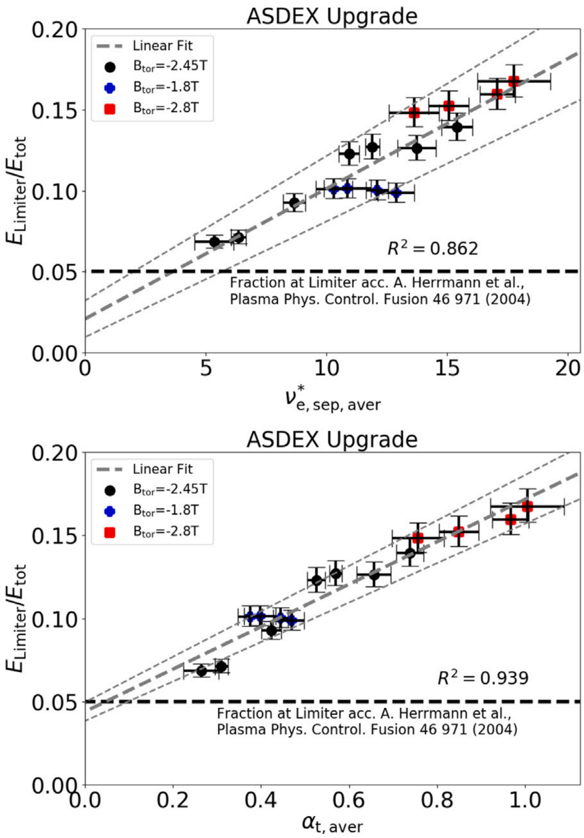

Fig. 4. Scaling of heat loads at the first wall of AUG for the entire database with different q_{95} ($B_{tor=-2.45T}$: black markers, $B_{tor=-1.8T}$: blue markers, $B_{tor=-2.8T}$: red markers) normalized against entire heat loads captured with the AUG cooling water calorimetry plotted against two separatrix parameters: the separatrix collisionality $\nu^*_{e,sep}$(definition acc. to Ref. [23]) (top plot) and the turbulence control parameter α_t (definition acc. to Ref. [24]) (bottom plot). Both parameters are obtained by using the Edge Thomson Scattering (TS) diagnostic at the outer midplane following the scheme as described in Ref. [24]. Both parameters are averaged over the time interval t=3.0–7.0s (where possible) in order to provide reasonable scaling values. The linear fit with uncertainty range and the correlation parameter R^2 are plotted. One can see that using α_t provides a clear, almost linear trend over the entire H-mode range of α_t ($0.1 \leq \alpha_t \leq 1.0$). (For interpretation of the references to colour in this figure legend, the reader is referred to the web version of this article.)

by the AUG cooling water calorimetry. This quantity can now be scaled against certain plasma parameters. It is rather practical to use a parameter related to filamentary transport. As known from previous works [25], the area close to the separatrix seems to be the key area to characterize filaments in the small ELM regime, therefore we focus on the separatrix as the key area to characterize the heat loads at the first wall. A common parameter characterizing filamentary transport is collisionality ν^*_e [11,13]. Previous attempts in L-modes compared divertor and midplane collisionality [13] in order to characterize the filamentary transport. As shown in Ref. [11], using divertor collisionality is not an appropriate parameter to scale filamentary transport in H-modes, which we suppose here also for heat loads caused by enhanced filamentary transport. In this work, we just use the midplane separatrix collisionality $\nu^*_{e,sep}$ as defined in Ref. [23]. The scheme to determine the required separatrix values from edge Thomson scattering is described in Ref. [24]. The scaling of the normalized first wall heat loads against $\nu^*_{e,sep}$ is shown in Fig. 4 (top). The R^2-parameter, a correlation coefficient, reveals a value of 0.862, a promising value. A linear regression is applied as well, the fit line and uncertainty range obtained from the regression is added. Looking at the profile, one can see that the B_{tor}-values −1.8T and −2.8T reveal a slight deviation from

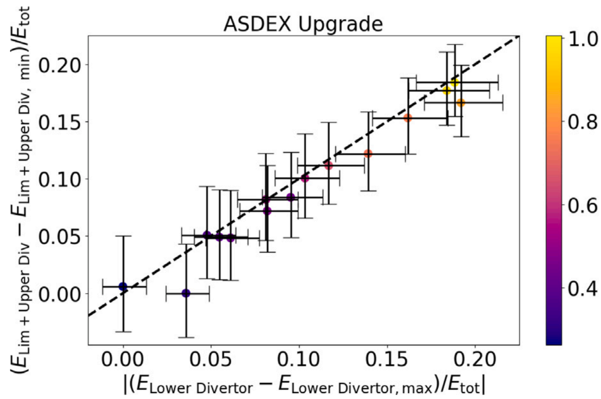

Fig. 5. The evolution of the fraction of deposited energy on the lower divertor (considering inner/outer divertor and roof baffle) is plotted against the evolution of the fraction of deposited on the first wall and the upper (inner/outer) divertor. Both parameters are normalized by the sum of the entire energy found by the KWK. The *x*-axis denotes the decrease at the lower divertor, the *y*-axis denotes the increase at the first wall and the upper divertor. The offset is set to 0 for both evolutions and the absolute value of the slope of the lower divertor evolution is used (the actual slope is negative, but done for better visualization). A colourmap is added visualizing the α_t-value of each shot. It can be clearly seen that with increasing α_t, the deposited energy in the lower divertor decreases and the decrease can almost entirely be found on the upper divertor and the first wall, on non-divertor components. From this observation, it seems that an enhanced filamentary transport changes the distribution of power depositions between divertor and non-divertor regions without substantially modifying the overall power loss. (For interpretation of the references to colour in this figure legend, the reader is referred to the web version of this article.)

the linear trend. Using collisionality seems not to be the best parameter to scale the first wall heat loads. Alternatively, the so-called turbulence control parameter α_t is tested, which is introduced in several works. We refer to the two latest ones [24,26]. As definition of α_t, we use the simplified formula as given in Ref. [24]:

$$\alpha_t \approx 3 \cdot 10^{-18} q_{cyl}^2 R_{geo} \frac{n_e}{T_e^2} Z_{eff}. \tag{3}$$

As clarified in Ref. [24], using the simplified formula is justified for AUG. The major difference between $\nu^*_{e,sep}$ and α_t is the q_{cyl}^2-dependence of α_t compared to the linear q_{cyl}-dependence of $\nu^*_{e,sep}$. In Fig. 4 (bottom), the heat load scaling with α_t is shown. The results of a linear regression are also plotted. Compared Fig. 4 (top), an almost linear trend can be observed over the entire range of α_t, even after the transition from the small ELM regime to a Type-I ELMy H-mode, which normally occurs for H-modes below $\alpha_t < 0.4$. R^2 provides a value of 0.939. We want to add here that the increase at the first wall is not related to an increased radiation due to the increased fuelling. As shown in Ref. [8], increasing fuelling in a small ELM equilibrium does not lead to a significant change in the radiation. Therefore, the increased heat loads at the first wall are indeed related to an increased radial filamentary energy transport. The scaling covers a range between ~ 0.25 and ~ 1.0 for α_t, whereas the first wall fraction covers a range between $\sim 6\%$ and 16%, an increase by an factor of almost 3 over the entire range of α_t for H-modes. This observation is consistent with an enhancement of the filamentary activity at higher α_t, when the plasma turbulence is dominated by resistive interchange modes originating at the separatrix. Additionally, the result for the first wall heat loads from Ref. [14] is added, at that time $\sim 5\%$ of the injected energy has been found in a low density ELMy H-mode with carbon walls in AUG and seems to be in good agreement with our observations. Due to the data quality of the edge TS at that time and lack of reasonable Z_{eff}-estimate in a carbon machine, no values for $\nu^*_{e,sep}$ or α_t can be provided. Instead a line over the entire x-range is added.

With the fuelling scans, we should also be able to observe with increasing fuelling a reduction of the transport down the divertor from

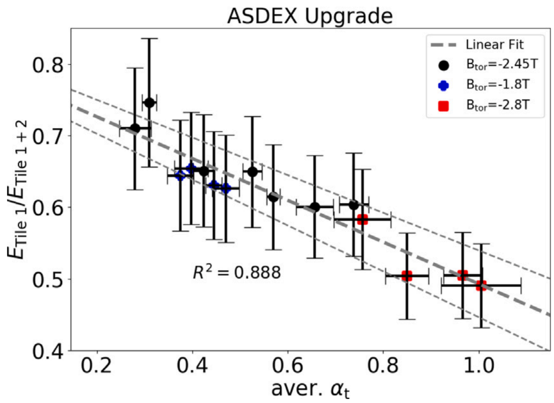

Fig. 6. Evolution of the energy deposition at the outer target at Tile 1 normalized against the sum of Tile 1 and Tile 2 against α_t. Corresponding labels for both tiles are taken from Fig. 1 (right). With increasing α_t, the energy found on Tile 1 decreases almost linearly from ~ 0.7 to ~ 0.5, corresponding to a decrease of the energy deposited on the outer target as observed by the cooling water calorimetry. (For interpretation of the references to colour in this figure legend, the reader is referred to the web version of this article.)

the calorimetric measurements and at the same time an increase of the heat loads on non-divertor components. In this case, we refer to the first wall and the upper divertor. According to Ref. [8], these areas are exposed to significant heat loads due to the enhanced filamentary transport. This would also prove that the reduction of heat loads at the lower divertor is not transferred to plasma radiation (which support the observation from Ref. [8]), but indeed into particle heat loads through radial filamentary transport on non-divertor components.

This evolution of the heat loads of the lower divertor (considering inner and outer divertors) against the evolution at dedicated non-divertor components (first wall and upper (inner and outer) divertor) can be proven with this dedicated database. For both areas (lower divertor and non-divertor components) the offsets are set to 0. For better illustration the absolute value of the slope of the lower divertor evolution is used. Fig. 5 presents that evolution. A colourmap is added showing the α_t-value of each marker. One can see a clear linear trend between both areas, from which one can conclude that the reduction of heat loads at the outer target leads to an increase of heat loads on non-divertor components in the same magnitude. From this observation, it seems that an enhanced filamentary transport does not cause a change in the power deposition, but rather a change in the distribution of the power deposition on the PFCs.

This evolution is also observed by means of thermocouple measurements at the outer target. As seen in Fig. 1 (right), the position of available thermocouples at the lower outer divertor is indicated. Two thermocouples are installed in the outer target ('Tile 1'), which provide one value. Additionally, a thermocouple is installed in the tile row ('Tile 2') above 'Tile 1'. 'Tile 1' and 'Tile 2' together define the lower outer divertor. To be able to resolve the heat load evolution, we normalize the heat loads found on 'Tile 1' against the sum of the heat loads found on 'Tile 1' and 'Tile 2' and plot them against α_t. The results are shown in Fig. 6. As seen previously, the heat load scaling reveals an similar linear trend with a significant reduction at 'Tile 1' covering the observation found in Fig. 5. We would like to add that any comparison between these two trends should be interpreted with care due to the different normalization factors of the data considered. The added R^2 parameter of the applied linear regression reveals a value of 0.888. It has to be added here that the approach on which the evaluation of the thermocouples is based on, has a quite high intrinsic uncertainty($\sim$ 17%). This may lead to a slightly reduced R^2. Checks with IR thermography and with j_{sat} from Langmuir probes indicate that the changed energy deposition due to the λ_q broadening does not reach 'Tile 2'. From this we can conclude that the observed reduction on 'Tile 1' corresponds to a reduced heat transport from the midplane down to the outer target due to the enhanced perpendicular filamentary transport.

4. Summary and next plans

First results of scaling the first wall heat loads in AUG have been presented. The reliability of the calorimetric measurements has been ensured by providing the global energy balance. The established database and the chosen shot setup allows a reliable assignment of measured heat loads to certain plasma parameters. The results suggest that the heat load follows the turbulence control parameter α_t almost linearly. Since database is based on H-modes, this scaling is only valid for the range between $0.1 < \alpha_t < 1.0$. The variation due to the safety factor q suggests that the separatrix collisionality $\nu^*_{e,sep}$ is not a suitable parameter to reflect correctly this aspect. On the basis of this study a redistribution of heat loads is observed with increasing α_t, where more heat loads reach non-divertor components through enhanced filamentary transport. This is in agreement with plasma turbulence being dominated by resistive interchange modes at the separatrix.

The next step will be an in-depth analysis of filamentary transport with the aid of dedicated diagnostics. To be able to compare the energy carried by filaments, it is planned to estimate the amount of radiative heat loads reaching the first wall using the code CHERAB [27]. The final goal will be to establish a generally valid scaling for the heat load for the first wall based on a larger database with different scenarios on AUG and to extend these measurements to further machines (TCV, JET) in order to provide a generalized multi-machine scaling of the first wall heat loads.

CRediT authorship contribution statement

A. Redl: Conceptualization, Methodology, Software, Formal analysis, Writing – original draft, Writing – review & editing, Visualization. **T. Eich:** Conceptualization, Methodology, Formal analysis, Writing – review & editing. **N. Vianello:** Conceptualization, Methodology, Writing – review & editing. **P. David:** Formal analysis. **the ASDEX Upgrade Team:** Funding acquisition. **the EUROfusion MST1 Team:** Funding acquisition.

Declaration of competing interest

The authors declare that they have no known competing financial interests or personal relationships that could have appeared to influence the work reported in this paper.

Data availability

Data will be made available on request.

Acknowledgements

The authors want to thank T. Hohman for his great support in recommissioning the calorimetric diagnostics of ASDEX Upgrade. This work has been carried out within the framework of the EUROfusion Consortium, funded by the European Union via the Euratom Research and Training Programme (Grant Agreement No 101052200 — EUROfusion). Views and opinions expressed are however those of the author(s) only and do not necessarily reflect those of the European Union or the European Commission. Neither the European Union nor the European Commission can be held responsible for them.

References

[1] T. Eich, B. Sieglin, A. Scarabosio, W. Fundamenski, R. Goldston, A. Herrmann, Phys. Rev. Lett. 107 (2011) 215001.

[2] T. Eich, A. Leonard, R. Pitts, W. Fundamenski, R. Goldston, T. Gray, A. Herrmann, A. Kirk, A. Kallenbach, O. Kardaun, A. Kukushkin, B. LaBombard, R. Maingi, M. Makowski, A. Scarabosio, B. Sieglin, J. Terry, A. Thornton, the ASDEX Upgrade Team, the JET EFDA Contributors, Nucl. Fusion 53 (2013) 093031.

[3] H. Zohm, Plasma Phys. Control. Fusion 38 (1996) 105.

[4] G. Federici, A. Loarte, G. Strohmayer, Plasma Phys. Control. Fusion 45 (2003) 1523.

[5] A. Loarte, G. Huijsmans, S. Futatani, L. Baylor, T. Evans, D.M. Orlov, O. Schmitz, M. Becoulet, P. Cahyna, Y. Gribov, A. Kavin, A.S. Naik, D. Campbell, T. Casper, E. Daly, H. Frerichs, A. Kischner, R. Laengner, S. Lisgo, R. Pitts, G. Saibene, A. Wingen, Nucl. Fusion 54 (2014) 033007.

[6] T. Eich, B. Sieglin, A. Thornton, M. Faitsch, A. Kirk, A. Herrmann, W. Suttrop, the JET contributors, the MST contributors, the ASDEX Upgrade, the MAST teams, Nucl. Mater. Energy 12 (2017) 84–90.

[7] G. Federici, C. Bachmann, L. Barucca, C. Baylard, W. Biel, L. Boccaccini, C. Bustreo, S. Ciattaglia, F. Cismondi, V. Corato, C. Day, E. Diegele, T. Franke, E. Gaio, C. Gliss, T. Haertl, A. Ibarra, J. Holden, G. Keech, R. Kembleton, A. Loving, F. Maviglia, J. Morris, B. Meszaros, I. Moscato, G. Pintsuk, M. Siccinio, N. Taylor, M. Tran, C. Vorpahl, H. Walden, J. You, Nucl. Fusion Fusion 59 (2019) 066013.

[8] M. Faitsch, T. Eich, G.F. Harrer, E. Wolfrum, D. Brida, P. David, M. Griener, U. Stroth, the ASDEX Upgrade Team, the Eurofusion MST1 Team, Nucl. Mater. Energy 26 (2021).

[9] M. Greenwald, Plasma Phys. Control. Fusion 44 (2002) R27.

[10] R. Goldston, M. Reinke, J. Schwartz, Plasma Phys. Control. Fusion 59 (2017) 055015.

[11] N. Vianello, D. Carralero, C. Tsui, V. Naulin, M. Agostini, I. Cziegler, B. Labit, C. Theiler, E. Wolfrum, D. Aguiam, S. Allan, M. Bernert, J. Boedo, S. Costea, H.D. Oliveira, O. Fevrier, J. Galdon-Quiroga, G. Grenfell, A. Hakola, C. Ionita, H. Isliker, A. Karpushov, J. Kovacic, B. Lipschultz, R. Maurizio, K. McClements, F. Militello, A. Nielsen, J. Olsen, J. Rasmussen, T. Ravensbergen, H. Reimerdes, B. Schneider, R. Schrittwieser, E. Seliunin, M. Spolaore, K. Verhaegh, J. Vicente, N. Walkden, W. Zhang, the ASDEX Upgrade Team, the TCV Team, the EUROfusion MST1 Team, Nucl. Fusion 60 (2020).

[12] M. Griener, E. Wolfrum, G. Birkenmeier, M. Faitsch, R. Fischer, G. Fuchert, L. Gil, G. Harrer, P. Manz, D. Wendler, U. Stroth, the ASDEX Upgrade Team, the EUROfusion MST1 Team, Nucl. Mater. Energy 25 (2020).

[13] D. Carralero, S. Artene, M. Bernert, G. Birkenmeier, M. Faitsch, P. Manz, P. de Marne, U. Stroth, M. Wischmeier, E. Wolfrum, The ASDEX Upgrade Team, The EURO-fusion MST1 Team, Nucl. Fusion 58 (2018) 096015.

[14] A. Herrmann, T. Eich, V. Rohde, C.J. Fuchs, J. Neuhauser, the ASDEX Upgrade team, Plasma Phys. Control. Fusion 46 (2004).

[15] T. Hohmann, A. Redl, V. Rohde, G. Schall, M. Schandrul, the ASDEX Upgrade Team, Fusion Eng. Des. 187 (2023) 113365.

[16] A. Redl, T. Hohmann, T. Eich, Vianello, P. David, G. Schall, S. Vorbrugg, V. Rohde, A. Herrmann, N. den Harder, M. Griener, the ASDEX Upgrade Team, the EUROfusion MST1 Team, 2022, submitted for publication.

[17] T. Richter, H. Vernickel, Rev. Sci. Instrum. 65 (1994).

[18] G. Matthews, Nucl. Mater. Energy 12 (2017) 227–233.

[19] A. Butland, R. Maddison, J. Nucl. Mater. 49 (1973) 45–56.

[20] P. Dorogokupets, E. Ponomarev, E. Melekhova, Petrology 7 (1998) 574–591.

[21] P. David, M. Bernert, T. Pütterich, C. Fuchs, S. Glöggler, T. Eich, the ASDEX Upgrade Team, Nucl. Fusion 61 (2021).

[22] F. Wagner, G. Fussmann, T. Grave, M. Keilhacker, M. Kornherr, K. Lackner, K. McCormick, E. Müller, A. Stäbler, G. Becker, K. Bernhardi, U. Ditte, A. Eberhagen, O. Gehre, J. Gernhardt, G. v. Gierke, E. Glock, O. Gruber, G. Haas, M. Hesse, G. Janeschitz, F. Karger, S. Kissel, O. Klüber, G. Lisitano, H.M. Mayer, D. Meisel, V. Mertens, H. Murmann, W. Poschenrieder, H. Rapp, H. Röhr, F. Ryter, F. Schneider, G. Siller, P. Smeulders, F. Söldner, E. Speth, K.-H. Steuer, Z. Szymanski, O. Vollmer, Phys. Rev. Lett. 53 (1984) 1453.

[23] S. Braginskii, Rev. Plasma Phys. 1 (1965) 205.

[24] T. Eich, P. Manz, R. Goldston, P. Hennequin, P. David, M. Faitsch, B. Kurzan, B. Sieglin, E. Wolfrum, the ASDEX Upgrade team, the EUROfusion MST1 team, Nucl. Fusion 60 (2020) 056016.

[25] G. Harrer, E. Wolfrum, M. Dunne, P. Manz, M. Cavedon, P. Lang, B. Kurzan, T. Eich, B. Labit, J. Stober, H. Meyer, M. Bernert, F. Laggner, F. Aumayr, the EUROfusion MST1 Team, the ASDEX Upgrade Team, Nucl. Fusion 58 (2018) 112001.

[26] T. Eich, P. Manz, the ASDEX Upgrade team, Nucl. Fusion 61 (2021) 086017.

[27] C. Giroud, A. Meakins, M. Carr, A. Baciero, C. Bertrand, CHERAB spectroscopy modelling framework (version v0.1.0), 2018, http://dx.doi.org/10.5281/zenodo.1206142, Zenodo.